aerospace

MDPI

Article

Experimental Investigation on Morphological Characteristics and Propulsion Performance of Typical Metals Ablated with Multipulse Nanosecond Laser

Hao Liu, Jifei Ye *, Mingyu Li and Heyan Gao

State Key Laboratory of Laser Propulsion & Application, Department of Aerospace and Technology, Space Engineering University, Beijing 101416, China; liuhao1717117@163.com (H.L.); merle_lee@outlook.com (M.L.); gaohy_s@163.com (H.G.)
* Correspondence: yjf1981@163.com

Abstract: For laser ablation micropropulsion technology with metal as the target to increase the total impulse, the effective utilization and supply of a working medium is a crucial aspect. In this research, the ablation characteristics and propulsion performance of the typical metal targets, copper and aluminum, ablated via nanosecond laser ablation are analyzed. Due to the low melting point of aluminum, the protrusion characteristics in the remelted area are more prominent. Its surface morphology has characteristics for height extremum and roughness that are higher than those of copper. Affected by the anisotropy of the rough surface, the absorbed energy decreases with increasing roughness. The impulse coupling coefficient of the metal decreases and stabilizes at about 6 $\mu N \cdot W^{-1}$. The specific pulse of aluminum obtains a minimum value of 603.6 s at 6000 pulses and improves with increasing pulses. The propulsion parameters of copper alters slightly under various working conditions, with a maximum specific impulse of 685 s.

Keywords: ablation morphology; laser propulsion; metal target; roughness

check for updates

Citation: Liu, H.; Ye, J.; Li, M.; Gao, H. Experimental Investigation on Morphological Characteristics and Propulsion Performance of Typical Metals Ablated with Multipulse Nanosecond Laser. *Aerospace* **2023**, *10*, 690. https://doi.org/10.3390/aerospace10080690

Academic Editors: John Sinko and Jae Hyun Park

Received: 29 May 2023
Revised: 28 July 2023
Accepted: 31 July 2023
Published: 3 August 2023

1. Introduction

Micropropulsion technology is a key technology in the application of space micro-/nanosatellites, which is a research hotspot in the field of space satellites [1–3]. Laser ablation micropropulsion technology has the characteristics of a light structure, small impulse element, and high specific impulse. The target is irradiated with a laser with a high repetition rate, and the thruster generates a continuously adjustable microthrust [4].

Common target working media include metal working media, polymer working media, and energetic working media [5–7]. Polymer working media are difficult to completely decompose during laser ablation, resulting in a low specific impulse. Energetic working media release chemical energy through their own chemical bond fracture to improve the propulsion performance. However, it is difficult to ensure material structure uniformity during the preparation of energetic working media, which is not conducive to the provision of a continuous and stable thrust. In addition, the carrier of the working medium target band does not participate in ablation, and the presence of dead weight reduces the utilization rate of the target band.

A laser ablation microthruster with a metal working medium has the advantages of a stable thrust and high specific impulse due to the uniform structure and high ablation ionization rate of metal, making it suitable for practical engineering applications and theoretically having the potential to improve propulsion efficiency [8].

A.V. Pakhomov [9] stated that the impulse coupling coefficient is proportional to the atomic weight of the metal for typical metals such as Cu, Al, Fe, Zn, and so on, but the specific impulse was opposite in the laser ablation experiment. Wen [10] investigated the wavelength and pulse width conditions that exist when the optimum solution for the aluminum impulse coupling coefficient exists. Saeed [11] examined the propulsion performance of three metal foil targets: Cu, Fe, and Al. Zhang [12] ablated metal targets using an ultrashort laser and analyzed the reasons for energy dissipation surrounding the light spot. Li [13] simulated the thermal interaction of the nanosecond laser ablation of aluminum with the finite volume method. The predicted ablation depth matched the experimental law. Daniel [14] studied the ultrashort laser working form that optimizes the propulsion performance when copper is used as an ablative working medium. Li [15] demonstrated the high propulsion efficiency of metal microspheres by irradiating stainless steel microspheres with the nanosecond laser output from optical fibers. Xu [16] analyzed the impact of different laser energies and pressures on the propulsion performance of zinc from the perspective of the impulse.

The choice of working medium determines the design of the supply strategy, which affects the optimization of the laser ablative microthruster. The first laser ablation microthruster prototype with a millisecond pulse width, developed by Phipps [17] in 2002, adopted the coiled working medium supply mode. In order to solve the issue of the insufficient strength of flexible substrates, which are prone to cracking and vibration [18], a two-dimensional supply method using a rigid substrate disc was proposed. Aluminum was used as the working medium to produce a specific impulse of 1120 s [19]. Zhu [20] compared the target utilization efficiency of circular and spiral paths in the disc-type supply process. The thruster developed by Gurin et al. [21] used the spiral method to scan the target. The laser microthruster designed by Lorbeer [22] makes use of an MEMS scanning mirror to enable the scanning and ablation of the working medium. While improving the supply methods, research on ablation with large spots was carried out to improve the utilization rate of the working medium. Eyett [23] examined the relationship between the spot size and laser ablation efficiency. Li [24] investigated how the structure of the expanding plume changed when copper was irradiated with a nanosecond laser in an atmospheric setting. Chaja [25] summarized the impact of the spot size on the specific removal rate under the conditions of ultrashort pulse laser ablation. The existing research and relatively mature laser microthruster prototypes, however, give less consideration to choosing an appropriate supply strategy to use metal working media.

Laser ablation micropropulsion technology with a metal working medium is a promising research direction. Under laser irradiation with large spots, laser surface ablation provides feasibility for reducing the dimensionality of the working fluid supply to achieve a one-dimensional supply, which has a significant impact on its engineering applications.

In this paper, a millimeter-level nanosecond laser beam is selected to ablate two typical metal working media, copper and aluminum, in a vacuum chamber under multipulse ablation conditions. Based on the summary of the ablation morphology characteristics, the propulsion performance under multipulse conditions is analyzed, which is helpful to improve the working efficiency and practical application of laser ablation micropropulsion technology.

2. Experimental Settings

2.1. Laser Ablation Process

The experimental facilities used in this study consisted of four parts: a nanosecond pulse laser system, a microimpulse measurement system, a laser confocal optical system, and an optical path system. The schematic diagram of the laser light source, optical path structure, and microimpulse measurement system is shown in Figure 1.

The ablation process of metal was achieved through a nanosecond pulse laser system with laser wavelengths and pulse widths of 1064 nm and 10 ns. During the experiment, the single-pulse laser energy was set to 500 mJ, and Figure 2 displays the mass distribution of the attenuated laser beam. The laser beam had the characteristic of a narrow energy rising edge, and although there were slight fluctuations, the peak energy of the laser was symmetrically distributed relative to the axis within the flat top range. The diameter of the spot on the target surface of the torsion beam was determined to be 3 mm by adjusting the relative position of the focusing lens in the optical path system. The multipulse laser's operating frequency was set to 5 Hz. There was a cooling interval of 60 s after continuous operation for 100 s to avoid heat deposition that could affect the torsion pendulum's inherent parameters and lead to measurement inaccuracies. In the experiment, a total of nine operating conditions, including 2000 to 18,000 pulses with 2000 intervals, were studied. To lessen uncertainty and error, five sets of experiments were repeated under a single operating state. The background pressure in the vacuum chamber was 10 Pa.

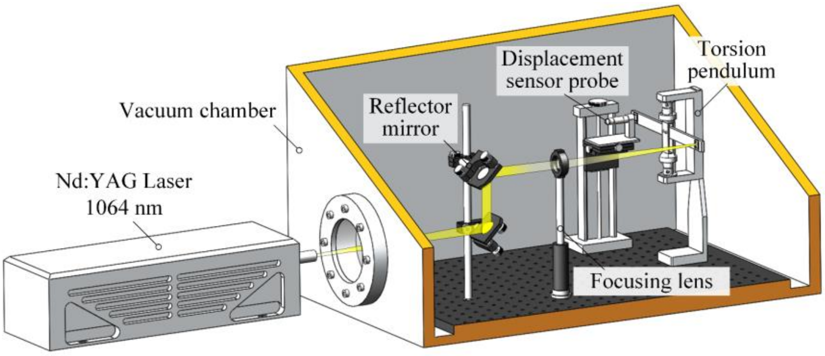

Figure 1. Schematic diagram of experimental system.

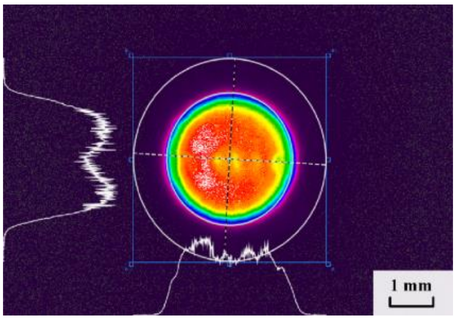

Figure 2. Mass distribution of nanosecond laser beam.

2.2. Materials

The experimental materials included cylinder-shaped over 99.9% pure metal targets made of Cu and Al. The physical properties of the two metals are listed in Table 1. The target surface had different morphologies after laser ablation with various pulse counts. With the help of an electronic balance with a resolution of 0.01 mg, the mass changes of ablated metal targets under various operating conditions were weighed. For example, the target masses at 1750 and 2250 pulses were measured as m_1 and m_2, and then the single ablation mass m at 2000 pulses was computed by $m = (m_2 - m_1)/500$.

Table 1. Physical properties of metals.

Metal	Melting Point (°C)	Boiling Point (°C)	First Ionization Energy ($\text{kJ}\cdot\text{mol}^{-1}$)	Resistivity (10^{-8} Ω·m, 20 °C)	Density ($\text{ng}\cdot\mu\text{m}^{-3}$)
Cu	1083	2580	745.5	1.75	8.96×10^{-3}
Al	660	2500	577.5	2.83	2.71×10^{-3}

2.3. Measurement Method

In the microimpulse measurement system, the torsion angle of the torsion pendulum beam, θ, was measured by displacement sensors. Figure 3 shows the impulse measurement torsion pendulum, mainly composed of precision flexible pivot, measuring beam, and high-precision displacement sensor. According to the theory of angular momentum [26–28], the microthrust caused the flexible pivot to rotate slightly. The maximum linear displacement after impulse loading could be measured through the displacement sensor, and its basic motion law can be explained through the following formula: T_0 represents the acting time of the external force, J is the inertia moment of the torsion pendulum, c is the damping coefficient, k is the stiffness coefficient of the pivot, the external force is represented by $f(t)$, and d is the arm of force acting through the external force. Formula (1) and the linear dependence of displacement are only valid when the torsion pendulum has a small amplitude.

$$\begin{cases} J\ddot{\theta} + c\dot{\theta} + k\theta = f(t)d & 0 < t < T_0 \\ J\ddot{\theta} + c\dot{\theta} + k\theta = 0 & t > T_0 \end{cases} \tag{1}$$

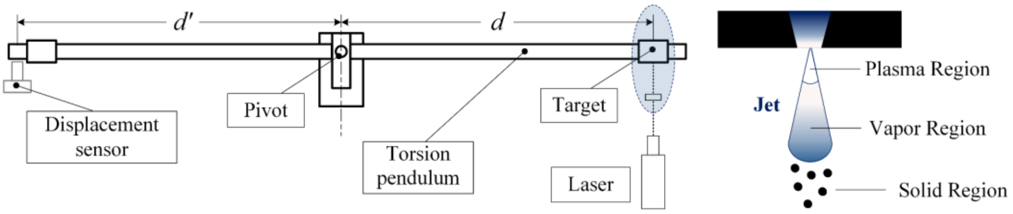

Figure 3. Schematic diagram of torsion pendulum.

The calculation method for the impulse obtained by converting the above torque balance formula within the time of external force action is shown in Formula (2):

$$I = \frac{k}{d \cdot d' \cdot \omega_n} s \tag{2}$$

where ω_n is the natural resonance frequency of the torsion pendulum, s is the maximum linear displacement measured by the sensor, and d' is the distance between the measurement point and the pivot. In this system, the measurement arm d' was 115 mm, and the ablation force arm d was 105 mm as shown in Figure 3.

The working parameters of the microimpulse measurement system were calibrated using the method proposed by Hong [29], and the linear relationship between impulse I and the maximum linear displacement s was obtained.

$$I = 0.1378 \cdot s \tag{3}$$

Impulse coupling coefficient C_m, specific impulse I_{sp}, and ablation efficiency η were selected to evaluate the propulsion performance. The impulse coupling coefficient C_m is defined as the ratio of laser-induced impulse to incident laser energy, and its calculation method is shown in Formula (4). The specific impulse I_{sp} characterizes the ability of the consumed working medium to provide impulse in the process of laser ablation propulsion. As shown in (5), I_{sp} is calculated by the ratio of the impulse obtained through a single pulse to the corresponding ablation weight. Δm represents the single-pulse ablation mass, and g is the gravity acceleration. Dimensionless parameter of ablation efficiency η is defined as the efficiency of converting laser pulse energy into plume kinetic energy. Formula (6) illustrates the interrelationships of the above propulsion parameters.

$$C_m = \frac{I}{W} \tag{4}$$

$$I_{sp} = \frac{I}{\Delta m g} \tag{5}$$

$$\eta = \frac{W_E}{W} = \frac{\Delta m v_E^2}{2W} = \frac{I_{sp} g C_m}{2} \tag{6}$$

The 3D measuring laser microscope OLS5100 manufactured by OLYMPUS was used to analyze the ablation morphologies of the target material under various working conditions. The microscope has two optical systems—color imaging and laser confocal—that enable it to acquire color and shape information as well as high-definition images. The optical system utilizes a 405 nm laser light source to automatically move the focus position during height measurement to obtain multiple confocal images, estimate the peak position of each pixel, and obtain 3D morphology information of the sample surface.

3. Results and Discussion

3.1. Analysis of Ablation Morphology

Three-dimensional images were collected by the laser confocal optical system to analyze the irregular contours of the ablation surface morphology of the target material. The color information and height distribution of the ablation pit are illustrated in Figures 4 and 5, respectively. The morphology characteristics of the copper and aluminum metal targets were compared when the pulses reached 2000. In the color image, it can be observed that, under the repeated impact of the laser pulse, the surface of Cu is relatively regular and presents a circular feature. The color image of Al directly displays the disordered morphology generated through condensation after melting. The aluminum target has circular protrusions on the outer edge of the ablation pit that are higher than the nonablated reference plane, which were not seen on the copper target, and there are also much more and higher protrusions distributed inside the ablation pit on the aluminum surface than on the copper surface according to the height distribution diagram in Figure 5. From a 2D viewpoint, it was discovered that, under same-sized-spot ablation, the area of the deformation area of Cu irradiated with a laser is smaller than that of Al as depicted by the dashed circle in Figure 5. A circular convex structure formed on the ablated Al's outside border after repeated pulse action.

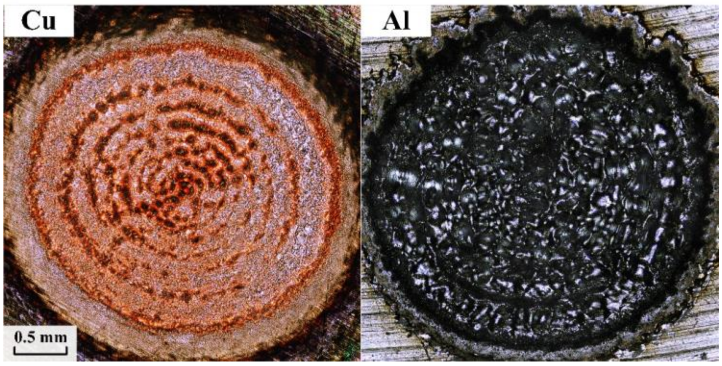

Figure 4. Color image of ablation morphology.

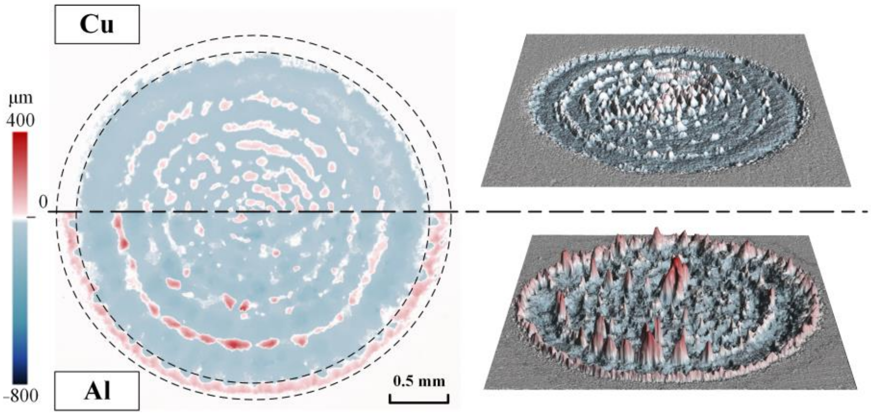

Figure 5. Height distribution of ablation morphology.

To further analyze the internal morphology, Figure 6 displays the axial contour statistics for the ablation pit with a pulse count of 2000. The diameter of the ablation pit of the copper target is 3082 µm. The diameter of the aluminum surface with morphology changes is 3387 µm nevertheless. The annular protrusion formed at the outer edge of the ablation area is 101 µm tall. In addition, with 2000 pulses, it was found that the morphology of the copper surface has denser protrusions near the center but a lower height than the aluminum surface.

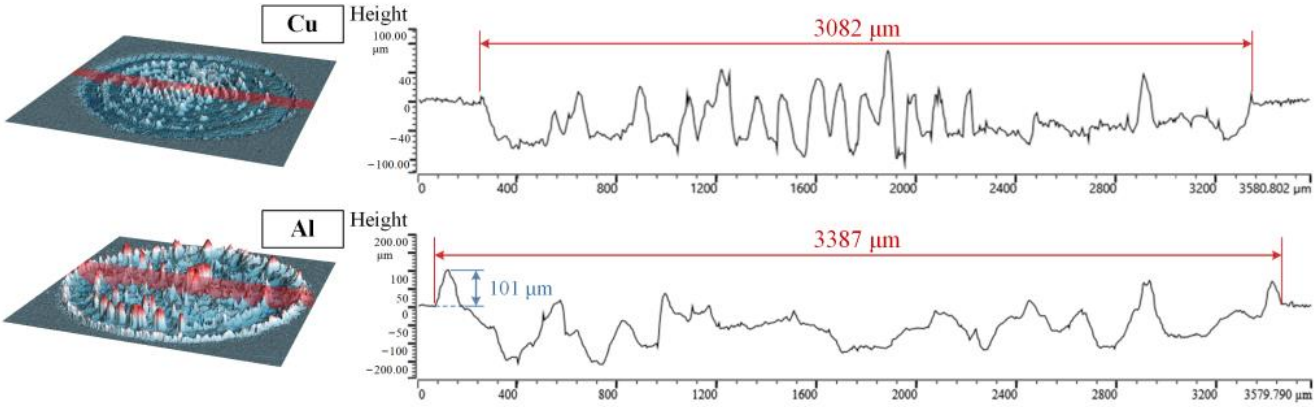

Figure 6. Distribution curve of height contour.

A shallow gasification mechanism is primarily responsible for the mass transfer of the metals exposed to nanosecond-pulse-width laser radiation. The rate of laser absorption directly affects how metals go through phase transition processes like melting and gasification. The Hagen–Rubens formula [30] is shown in (7), which can be used to calculate the absorption rate of metals for lasers with 1064 nm. The electrical resistivity under 20 °C is listed in Table 1. Al has a higher metal resistivity and a faster rate of energy absorption from the laser pulse than Cu. Al also has a lower melting point than Cu. As a result, the temperature of Al increases in response to repeated pulses, but there is no effective heat dissipation medium in a vacuum environment, resulting in the presence of molten metal in the high-temperature regions of the ablation pit. It is challenging to convert all of the molten aluminum into gaseous or plasma states due to the laser energy density of the huge light spot, which is 7 J/cm^2. As the number of pulses increases, the proportion of molten aluminum that splashed out into the plume increases, and it rapidly cools to form a remelting protrusion phenomenon when the pulse laser stops working.

$$A(T)_{Nd:YAG} = 354.67\sqrt{\rho(T)} \tag{7}$$

Figure 7 displays the 2D height distribution map of the ablation morphology for several-nanosecond laser pulses. The remelting protrusion inside the ablation pit shows a ring spacing distribution, which is related to the mass distribution of the beam. The greater melting point of copper makes it more noticeable on its surface. The highest and deepest values in the ablation morphology are shown in Figure 8. On the surfaces of the two typical metal targets, the ablation depth and height of the remelting protrusions gradually rise with the pulse. At 10,000 pulses, the maximum height of aluminum's surface morphology decreases, and it stabilizes at around 600 µm; the maximum depth of the ablation pit is around 1000 µm, and it does not decrease further.

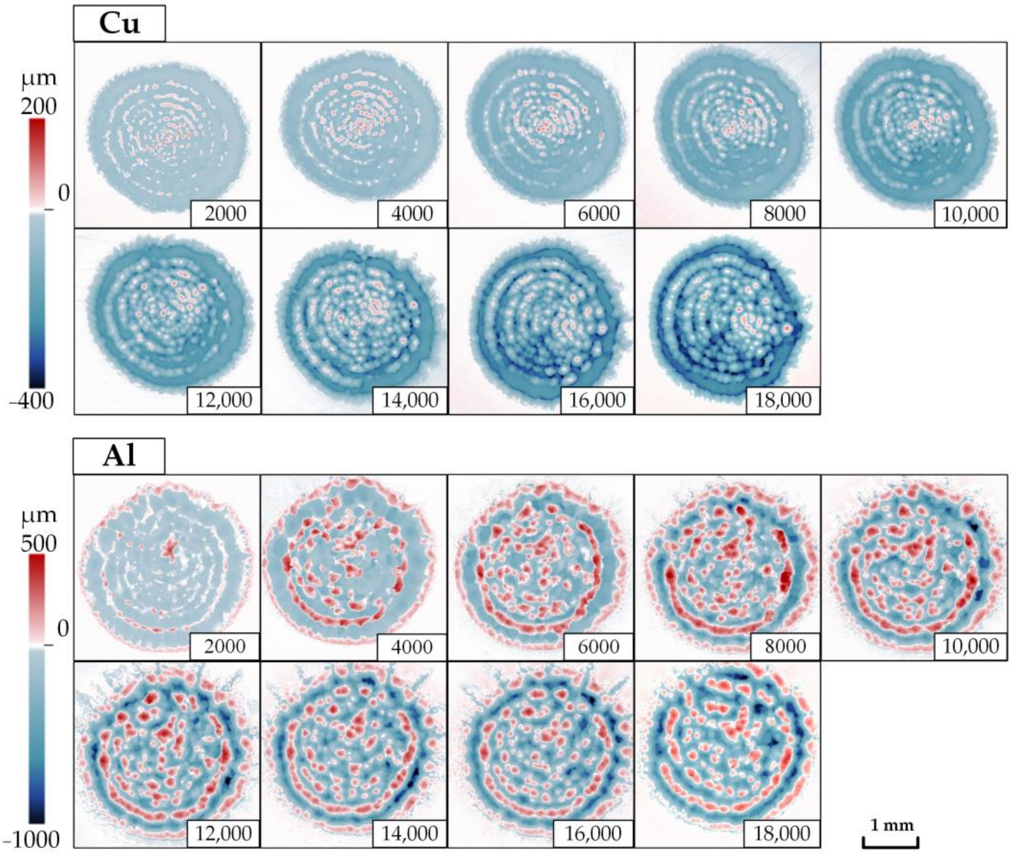

Figure 7. Ablation morphology height versus the number of pulses.

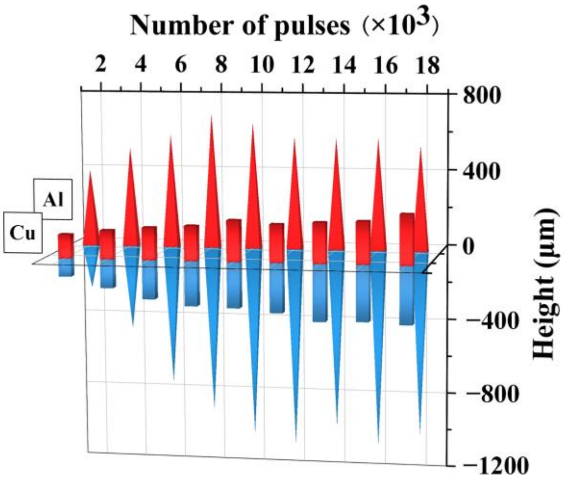

Figure 8. Height extremum versus the number of pulses.

Parameters such as root mean square height *Sq*, skewness *Ssk*, and kurtosis *Sku* were selected to describe the roughness of the ablation surface, which can be calculated as follows:

$$Sq = \sqrt{\frac{1}{A}\iint_A Z^2(x,y)dxdy} \tag{8}$$

$$Ssk = \frac{1}{Sq^3}\left[\frac{1}{A}\iint_A Z^3(x,y)dxdy\right] \tag{9}$$

$$Sku = \frac{1}{Sq^4}\left[\frac{1}{A}\iint\limits_A Z^4(x,y)dxdy\right] \quad (10)$$

Sq is defined as the root mean square of the height of each point in the target area A, which is equivalent to the standard deviation of the height. *Ssk* is frequently used to assess the roughness of the shape, that is, the concave–convex tendency of the surface. The value of *Ssk* is negative or positive to indicate the height distribution relative to the base plane. *Sku* is a parameter used to determine how sharp a rough shape is.

Figure 9 shows the trend of the surface roughness parameter *Sq* as the number of laser pulses increases. For Cu, the root mean square height of the ablation morphology increases linearly with the pulse counts, but the overall value is modest. When the number of pulses reaches 18,000, the *Sq* of the ablation pit is 99.9 µm. The ablation surface of Al is more complex and has a higher roughness. The effect of the increasing pulses on the surface roughness can be disregarded once the number of laser pulses reaches 8000 or more because the rate of increase of the root mean square height rapidly declines.

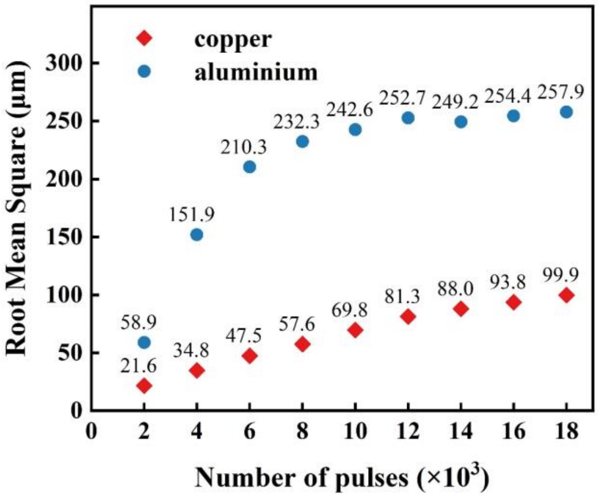

Figure 9. Root mean square versus the number of pulses.

The roughness parameters of the ablation pits, skewness and kurtosis, are, respectively, listed in Figures 10 and 11. Figure 10 shows that the development laws of the two metals are similar. The height distribution of the ablation pits is lower than the average under the condition of few pulses. The morphology becomes more dominated by the remelting protrusion phenomena as the pulse count rises, resulting in a gradually rising height distribution. In Figure 11, both Cu and Al exhibit strong sharpness on the ablated surface after 2000 pulses, which rapidly decreases after 4000 pulses. The *Sku* of the surface of Cu is basically steady and is less affected by the number of pulses. After 8000 pulses, the *Sku* of the ablation surface of Al is stable at three, indicating that the height of the ablation morphology follows the normal distribution currently, while the height distribution of the copper surface is relatively flat.

3.2. Analysis of Propulsion Performance

In order to study the impact of the typical metal morphology characteristics on the propulsion performance, while keeping the laser energy condition unchanged, this paper used a microimpulse measurement system to compare the impulse of the ablation morphology obtained with different pulse counts. Figure 12 represents the C_m of the two metal target's ablation pits under laser action as the number of pulses increases. There is a general trend toward a negative development. Under the action of a single-pulse laser, the C_m values generated on the smooth metal surfaces of copper and aluminum are 30.54 µN/W and 25.74 µN/W. For the ablation morphology under the action of multiple pulses, the C_m

obtained on the rough surface rapidly decreases. The C_m of the various working media varies when the pulse count is 2000, and the C_m produced by the surface morphology of Al is 10.10 µN/W compared to a value of 7.22 µN/W for Cu.

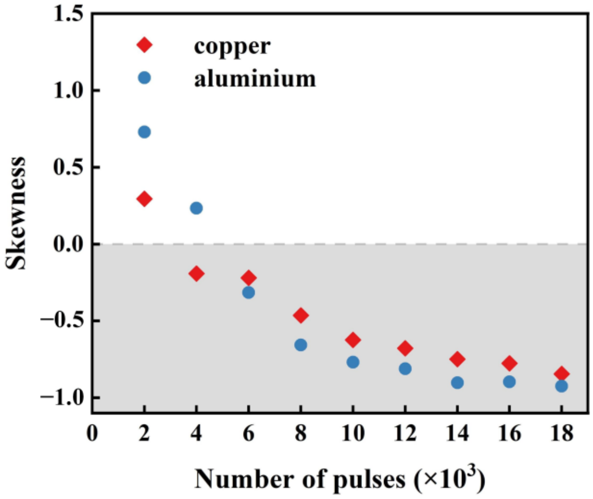

Figure 10. Skewness versus the number of pulses.

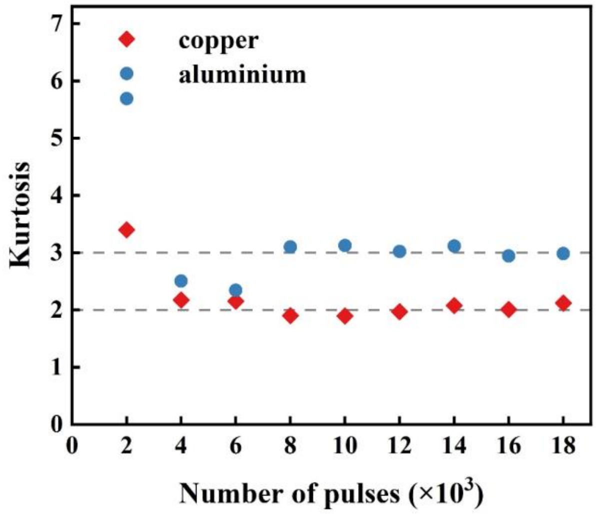

Figure 11. Kurtosis versus the number of pulses.

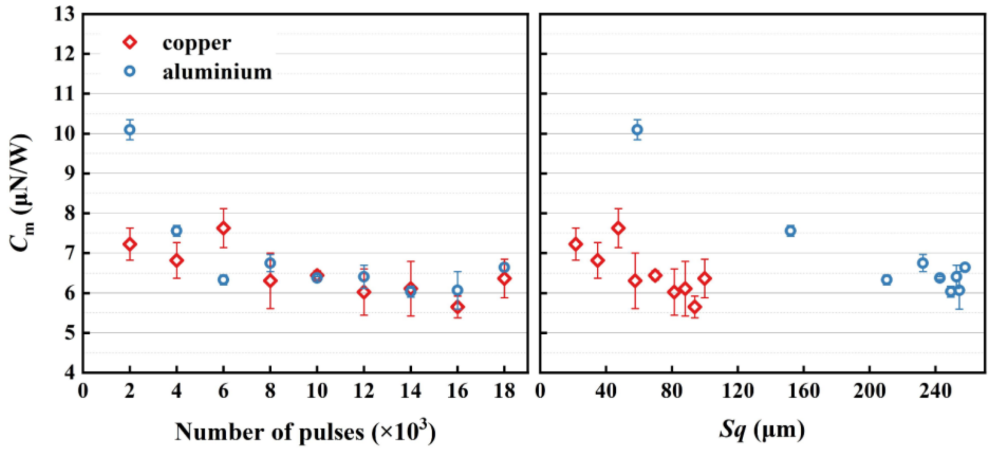

Figure 12. The effect of laser pulses and roughness on C_m.

The roughness of the ablation morphology is connected to the propulsion performance under various working conditions. In Figure 12, an impulse coupling coefficient scatter distribution map is created using the root mean square height for various pulse counts as the independent variable. As the surface roughness increases, the C_m of the metal targets gradually decreases. Less laser energy contributes to propulsion when the roughness of Al reaches 200 μm or higher or when there have been more than 6000 repeated pulses. However, owing to the low melting point and the first ionization energy, Al tends to be peeled off to generate an impulse. As a result, the two metals' difference in roughness becomes more noticeable as the pulses grow, yet the targets' C_m values are similar and basically stable at 6 $\mu N \cdot W^{-1}$.

Figure 13 shows the distribution of I_{sp}. The I_{sp} of the various ablation morphologies for Cu varies, but it always ranges between 300 and 700 s. Al produces more I_{sp}, which is higher than Cu. At 2000 pulses, due to the large impulse of the target material, it reaches 873.1 s. As the impulse decreases, the minimum I_{sp} reaches its minimum value of 603.6 s at 6000 pulses. The impulse obtained with Al is basically stable with increased pulses; however, an improvement in the surface roughness is accompanied by a drop in the single ablation mass as shown in Figure 14. As a result, the increased I_{sp} generated by Al reaches a maximum value of 1232.3 s at 18,000 pulses.

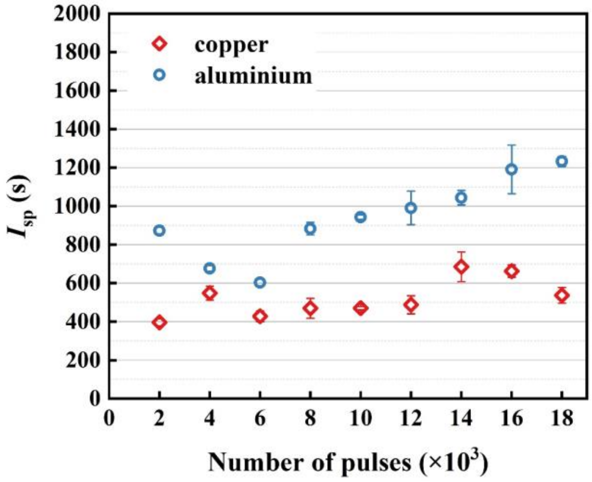

Figure 13. Specific impulse versus the number of pulses.

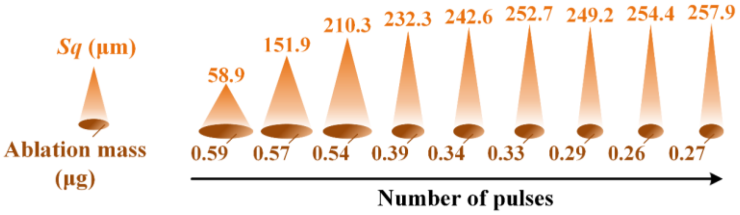

Figure 14. The ablation characteristics of Al.

It is worth noting that the experimental results help to qualitatively analyze the trend of I_{sp}'s change with respect to the pulse number. In the experiment, when the target surface is impacted by multiple pulses in a vacuum environment, the splashed metal powder attaches to the target again, affecting the weight and causing the specific impulse calculation to be higher.

The correlation between the ablation efficiency and pulse number is depicted in Figure 15. A lower level of metal ablation efficiency is produced in this situation due to the laser's low energy density. According to the analysis of the ablation morphology and specific impulse distribution, the ablation efficiencies of Cu with different laser pulses are less than 2%, which is generally lower than the results of Al. The I_{sp} of Al increases with the number of pulses, which improves the ablation efficiency of the working medium. As a result, the plume gains more kinetic energy with the same laser energy density, reaching the high value of 4.01% at 18,000 pulses. The figure also shows that the large impulse generated by Al under the action of 2000 pulses improves the ablation efficiency.

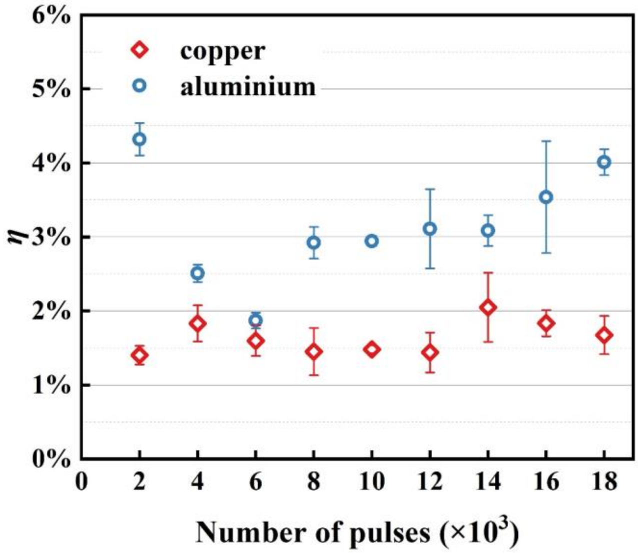

Figure 15. Ablation efficiency versus the number of pulses.

4. Conclusions

The working media of Cu and Al were multipulse-ablated with a nanosecond laser with a wavelength of 1064 nm and a pulse width of 10 ns. The height contour and roughness of the ablation pits were summarized, and the impact of the morphology on the propulsion performance was studied by using a torsion pendulum. The main conclusions are summarized as follows:

(1) The molten metal is difficult to entirely evaporate or ionize when the low-energy-density light spot pulses a metal target repeatedly, leading to the formation of a remelted protrusion. Due to the physical characteristic of a low melting point, the height extremum inside the ablation pit of Al is greater than that of Cu. Its deformation area under multipulse irradiation is larger, and the circular protrusion appears at the outer edge of the pit.

(2) The *Sq* of Cu shows a linear growth relationship with the number of laser pulses, with a value of 99.9 μm at 18,000 pulses, but this is still significantly less than that of 257.9 μm, which was found for the surface morphology of Al. When the number of pulses exceeds 8000, it is worth noting that the roughness of aluminum's surface morphology is greater than 200 μm with a declined growth rate. The *Sku* of the aluminum surface maintains a value of three, reflecting that the height contour within the ablation morphology follows the normal distribution, while the contour of Cu is relatively flat.

(3) The C_m of the two metals continuously decreases as the roughness of the morphology increases. Under various pulse numbers, the S_q of the copper surface is below 100 μm, and the I_{sp} distribution is between 300 and 700 s, with a small amplitude for the propulsion parameter. Due to changes in the single ablation mass, as the number of pulses increases, the impulse generated by Al gradually stabilizes, but the I_{sp} shows a gradually increasing trend.

The propulsion performance of copper and aluminum tends to stabilize under multipulse action and is closely related to the morphology characteristics of the ablation pits. In the future, we will carry out multipulse laser ablation experiments using other metal working media and nonmetallic materials as the research objects, we will summarize the performance characteristics of different working media, and we will optimize the performance of laser thrusters.

Author Contributions: Conceptualization, J.Y. and H.L.; methodology, M.L. and H.G.; formal analysis, M.L.; investigation, H.L.; writing—original draft preparation, H.L.; writing—review and editing, J.Y. and H.L. All authors have read and agreed to the published version of the manuscript.

Funding: This research received no external funding.

Data Availability Statement: Not applicable.

Conflicts of Interest: The authors declare no conflict of interest. The funders had no role in the design of the study; in the collection, analyses, or interpretation of the data; in the writing of the manuscript; or in the decision to publish the results.

References

1. Zhang, K.L.; Chou, S.K.; Ang, S.S. Development of a solid propellant microthruster with chamber and nozzle etched on a wafer surface. *J. Micromech. Microeng.* **2004**, *14*, 785–792. [CrossRef]
2. Mueller, J. Thruster Options for Microspacecraft: A Review and Evaluation of Existing Hardware and Emerging Technologies, of Aiaa Progress in Astronautics & Aeronautics Chapter Aiaa. In Proceedings of the 33rd Joint Propulsion Conference and Exhibit, Seattle, WA, USA, 6–9 July 1997.
3. Mueller, J. Thruster Options for Microspacecraft: A Review and Evaluation of State-of-the-Art and Emerging Technologies. In *Micropropulsion for Small Spacecraft*; American Institute of Aeronautics and Astronautics: Reston, VA, USA, 2000.
4. Phipps, C.; Luke, J.; Helgeson, W. Laser space propulsion overview. In *Advanced Laser Technologies*; International Society for Optics and Photonics: Bellingham, WA, USA, 2007.
5. Lippert, T.; Hauer, M.; Phipps, C.R.; Wokaun, A. Fundamentals and applications of polymers designed for laser ablation. *Appl. Phys. A* **2003**, *77*, 259–264. [CrossRef]
6. Phipps, C.R.; Luke, J.R.; McDuff, G.G.; Lippert, T. Laser-Driven Micro-Rocket. *Appl. Phys. A* **2003**, *77*, 193–201. [CrossRef]
7. Urech, L. Design and Characterization of Energetic Polymers Applied in Laser Space Propulsion. Ph.D. Thesis, ETH Zurich, Zürich, Switzerland, 2007.
8. Phipps, C.; Bohn, W.; Lippert, T.; Sasoh, A.; Schall, W.; Sinko, J. Review: Laser-Ablation Propulsion. *J. Propuls. Power* **2010**, *26*, 609–637. [CrossRef]
9. Pakhomov, A.V.; Thompson, S.M.; Gregory, D.A. Ablative laser propulsion: A study of specific impulse, thrust and efficiency. *AIP Conf. Proc.* **2003**, *664*, 194–205.
10. Wen, M.; Li, N.; Wu, J. Experimental study on impulse coupling characteristics of 532 nm/1064 nm laser ablated Al target. *Infrared Laser Eng.* **2017**, *46* (Suppl. S1), 30–34. (In Chinese)
11. Saeed, H.; Jamil, Y.; Younas, A.; Shahid, M. Quantitative Measurements of Ablative Laser Propulsion Parameters of Metal Foils Using Pulsed Nd: YAG Laser. *Arab. J. Sci. Eng.* **2022**, *47*, 895–901. [CrossRef]
12. Zhang, N.; Wang, W.; Zhu, X.; Liu, J.; Xu, K.; Huang, P.; Zhao, J.; Li, R.; Wang, M. Investigation of ultrashort pulse laser ablation of solid targets by measuring the ablation-generated momentum using a torsion pendulum. *Opt. Express* **2011**, *19*, 8870–8878. [CrossRef]
13. Li, Y.; Ou, Y.; Wu, J.; Zhang, Y. Dynamic simulation on laser-metal interaction in laser ablation propulsion considering moving interface, finite thermal wave transfer, and phase explosion. *Acta Astronaut.* **2023**, *208*, 27–35. [CrossRef]
14. Forster, D.J.; Faas, S.; Weber, R.; Graf, T. Thrust enhancement and propellant conservation for laser propulsion using ultra-short double pulses. *Appl. Surf. Sci.* **2020**, *510*, 145391. [CrossRef]
15. Li, H.; He, Y.; Sun, J.; Zhang, Z.; Ge, Y. Metal microspheres propelled by shock wave based on the fiber structure laser propulsion. *Opt. Commun.* **2022**, *508*, 127695. [CrossRef]
16. Xu, Y.; Yang, L.; Zhou, D.; Li, Q.; Shi, W.; Jin, Y. A comparative study on the characteristics of nanosecond laser ablation zinc and acrylonitrile butadiene styrene targets. *J. Phys. D Appl. Phys.* **2023**, *56*, 135201. [CrossRef]
17. Phipps, C.R.; Luke, J.R.; McDuff, G.G.; Lippert, T. Laser-ablation-powered mini-thruster. *High-Power Laser Ablation IV SPIE* **2002**, *4760*, 833–842.
18. Phipps, C.R.; Luke, J.R.; Helgeson, W.; Johnson, R. Performance Test Results for the Laser-Powered Microthruster. *AIP Conf. Proc. Am. Inst. Phys.* **2006**, *830*, 224–234.
19. Ye, J.F.; Hong, Y.J.; Li, N.L. Laser ablation microthruster and its performance test. In Proceedings of the 38th Technical Exchange Conference and the 2nd Joint Conference on Space and Space Power of China Aerospace Third Professional Information Network, Dalian, China, 24–26 August 2017; pp. 37–43.
20. Zhu, C.; Ye, J.; Wang, Y. Comparison of target utilization rate of two paths for disc-type laser ablation micro thruster. In Proceedings of the Seventh Asia Pacific Conference on Optics Manufacture and 2021 International Forum of Young Scientists on Advanced Optical Manufacturing (APCOM and YSAOM 2021), Shanghai, China, 28–31 October 2021; Volume 12166, pp. 380–385.

21. Gurin, A.V.; Kuvaev, K.Y.; Loktionov, E.Y.; Protasov, Y.S.; Sirenko, K.N.; Zakharov, V.I. First attempt of a laser thruster space flight test: Lost at launch. *Opt. Laser Technol.* **2019**, *120*, 105656. [CrossRef]
22. Lorbeer, R.A.; Weixler, S.; Bauer, T.; Scharring, S.; Eckel, H.A. Single printed circuit board laser ablative thruster. In Proceedings of the 10th Pico and Nano Satellite Workshop, Würzburg, Germany, 13–14 September 2017.
23. Eyett, M.; Bäuerle, D. Influence of the beam spot size on ablation rates in pulsed-laser processing. *Appl. Phys. Lett.* **1987**, *51*, 2054–2055.
24. Li, X.; Wei, W.; Wu, J.; Jia, S.; Qiu, A. The influence of spot size on the expansion dynamics of nanosecond-laser-produced copper plasmas in atmosphere. *J. Appl. Phys.* **2013**, *113*, 243304. [CrossRef]
25. Chaja, M.; Kramer, T.; Neuenschwander, B. Influence of laser spot size and shape on ablation efficiency using ultrashort pulse laser system. *Procedia CIRP* **2018**, *74*, 300–304. [CrossRef]
26. Chakraborty, S.; Courtney, D.G.; Shea, H. A 10 nN resolution thrust-stand for micro-propulsion devices. *Rev. Sci. Instrum.* **2015**, *86*, 115109. [CrossRef]
27. Hathaway, G. Sub-micro-Newton resolution thrust balance. *Rev. Sci. Instrum.* **2015**, *86*, 105116. [CrossRef]
28. Asakawa, J.; Nishii, K.; Nakagawa, Y.; Koizumi, H.; Komurasaki, K. Direct measurement of 1-mN-class thrust and 100-s-class specific impulse for a CubeSat propulsion system. *Rev. Sci. Instrum.* **2020**, *91*, 035116. [PubMed]
29. Hong, Y.; Li, D.; Feng, X.; Jin, X.; Wang, S. *Measurement and Evaluation Methods of Satellite Microthruster Propulsion Performance*; Science Press: Shanghai, China, 2021.
30. Xie, J.; Kar, A.; Rothenflue, J.A.; Latham, W.P. Temperature-dependent absorptivity and cutting capability of CO2, Nd: YAG and chemical oxygen–iodine lasers. *J. Laser Appl.* **1997**, *9*, 77–85.